

PREPARED FOR SUBMISSION TO JCAP

# Axion minicluster power spectrum and mass function

---

**Jonas Enander, Andreas Pargner, Thomas Schwetz**

*Institut für Kernphysik, Karlsruher Institut für Technologie (KIT), 76021 Karlsruhe, Germany*

*E-mail:* [andreas.pargner@kit.edu](mailto:andreas.pargner@kit.edu)

**ABSTRACT:** When Peccei-Quinn (PQ) symmetry breaking happens after inflation, the axion field takes random values in causally disconnected regions. This leads to fluctuations of order one in the axion energy density around the QCD epoch. These over-densities eventually decouple from the Hubble expansion and form so-called miniclusters. We present a semi-analytical method to calculate the average axion energy density, as well as the power spectrum, from the re-alignment mechanism in this scenario. Furthermore, we develop a modified Press & Schechter approach, suitable to describe the collapse of non-linear density fluctuations during radiation domination, which is relevant for the formation of axion miniclusters. It allows us to calculate the double differential distribution of gravitationally collapsed miniclusters as a function of their mass and size. For instance, assuming a PQ scale of  $10^{11}$  GeV, minicluster masses range from about  $5 \times 10^{-16}$  to  $3 \times 10^{-13}$  solar masses and have sizes from about  $4 \times 10^4$  to  $7 \times 10^5$  km at the time they start to collapse.

arXiv:1708.04466v2 [astro-ph.CO] 8 Jan 2018

---

## Contents

<b>1</b>	<b>Introduction</b>	<b>1</b>
<b>2</b>	<b>Axion preliminaries and goals of this work</b>	<b>2</b>
<b>3</b>	<b>Axion energy density and power spectrum</b>	<b>4</b>
3.1	Initial conditions	4
3.2	The average energy density	6
3.3	Axion energy density power spectrum	8
<b>4</b>	<b>The size and mass of axion miniclusters</b>	<b>11</b>
4.1	Spherical collapse model	12
4.2	Double differential mass function	13
4.3	Minicluster mass and size distribution	15
<b>5</b>	<b>Discussion and Summary</b>	<b>19</b>
5.1	Adopted assumptions and limitations	20
5.2	Outlook and comments on observational consequences	21
<b>A</b>	<b>Solving the equation of motion</b>	<b>22</b>

---

## 1 Introduction

The QCD axion [1, 2] is one of the most attractive candidates for the dark matter in the Universe. It is the Goldstone boson related to a global  $U(1)$  symmetry, which is spontaneously broken at the Peccei-Quinn (PQ) scale  $f_{\text{PQ}}$  [3, 4], much larger than the electro-weak scale. Around the QCD scale the symmetry is explicitly broken by the potential created by QCD instanton effects. Axions are produced by various mechanisms in the early Universe and hence they can potentially account for the dark matter, see Refs. [5, 6] for reviews of axion cosmology.

In this work we are interested in the situation where the PQ phase transition happens after the end of inflation. In this case the axion field takes on random values in causally disconnected regions. It was noted by Hogan and Rees in Ref. [7] that this implies isocurvature fluctuations of order one in the axion energy density at the QCD phase transition, leading to so-called *axion miniclusters*. These are gravitationally bound systems of axions, whose mass is determined roughly by the size of the horizon at the QCD phase transition. The formation of axion miniclusters has been studied numerically by Kolb and Tkachev [8, 9], and later by Zurek, Hogan, Quinn [10]. For more recent work on axion miniclusters see Refs. [11–16]. Naive estimates indicate a typical minicluster mass of

$10^{-13}M_{\odot}$ , see e.g. Refs. [12, 17, 18] (we are going to address this number in detail below). If a significant fraction of axion dark matter is bound in those objects, severe implications for dark matter axion searches are expected. If dark matter resides in compact objects of order  $10^{-13}M_{\odot}$ , the probability that such an object passes through a detector at earth is very low, reducing dramatically the discovery potential of axion haloscopes, see for instance Refs. [19, 20]. Lensing signals have been discussed in Ref. [21], and recently in Refs. [15, 16].

In this work we develop semi-analytic methods to understand the formation of axion miniclusters and their distribution in mass and size. We restrict our analysis to the axion energy density produced by the so-called re-alignment mechanism, i.e., a classical, coherently oscillating axion field. Furthermore, we limit our analysis to the harmonic approximation of the potential. While those assumptions clearly capture only part of the full picture, our results do provide a useful estimate of the properties of the minicluster distribution generated by the re-alignment mechanism. It allows to identify important parameters and study in a transparent way the underlying physics. It will be a useful starting point for quantitative numerical studies of axion minicluster formation, as well as the subsequent evolution after decoupling from the Hubble flow.

The outline of this work is as follows. In section 2 we set the stage by reviewing the post-inflationary axion scenario and give a more concise description of the scope of this work. In section 3 we present a calculation of the average axion energy density including a consistent treatment of gradient terms, and we derive the power spectrum of the axion energy density fluctuations. In section 4 we develop a formalism to describe the gravitational collapse of the axion over-densities, which are non-linear from the very beginning. We present the double differential number density in mass and size of gravitationally bound clumps of axion energy density around the time of matter-radiation equality. Section 5 contains the summary and discussion of our results. In appendix A we describe our method to solve the equation of motion of the axion field.

## 2 Axion preliminaries and goals of this work

The random values of the axion field in causally disconnected regions in the post-inflation scenario leads to a network of cosmic strings, with on average one string per Hubble volume. As the Universe expands, gradient terms will smooth the axion field on scales of the horizon. The presence of the topological strings plays a crucial role in the evolution of the massless field [22]. Once the axion mass turns on due to QCD effects at temperatures around 1 GeV the string and domain wall network quickly decays [23, 24] and will provide a substantial fraction of the energy density in axions, subject to large uncertainties, see Refs. [25, 26] for numerical simulations. In the following we focus on the axions created due to the re-alignment mechanism (i.e., coherent field oscillations), neglecting the contribution of strings and domain walls to the average energy density as well as to inhomogeneities. While keeping in mind that this can only be part of the real picture, it is still useful to isolate the contribution of the re-alignment mechanism and study its properties.

Let us define the dimensionless field describing the axion as  $\theta(\vec{x}, t) = A(\vec{x}, t)/f_{\text{PQ}}$ , where  $A(\vec{x}, t)$  is the real scalar field. The equation of motion for  $\theta(\vec{x}, t)$  in the expanding

Universe is given by

$$\ddot{\theta} + 3H(T)\dot{\theta} - \frac{\nabla^2}{a^2}\theta + V'(\theta, T) = 0. \quad (2.1)$$

Here the dot denotes derivative with respect to time,  $\nabla$  is the derivative with respect to co-moving coordinates,  $H(T) = \dot{a}/a$  is the expansion rate with the cosmic scale factor  $a$ , and  $V(\theta, T)$  is the temperature dependent axion potential, and the prime denotes derivative with respect to  $\theta$ . The potential is related to the topological susceptibility of QCD,  $\chi(T)$ , by

$$V(\theta, T) = \frac{\chi(T)}{f_{\text{PQ}}^2}(1 - \cos \theta). \quad (2.2)$$

For small  $\theta$  the cosine can be expanded and we obtain the temperature dependent axion mass in terms of the susceptibility:

$$V(\theta, T) \approx \frac{1}{2}m^2(T)\theta^2, \quad m^2(T) = \frac{\chi(T)}{f_{\text{PQ}}^2}. \quad (2.3)$$

For  $T \lesssim 100$  MeV,  $\chi(T)$  becomes constant and the axion reaches its zero-temperature mass  $m_0$ . Approximately we have [1]

$$m_0 \simeq \frac{m_\pi f_\pi}{f_{\text{PQ}}} \frac{\sqrt{m_u m_d}}{m_u + m_d} \simeq 5.7 \times 10^{-6} \text{ eV} \frac{10^{12} \text{ GeV}}{f_{\text{PQ}}}, \quad (2.4)$$

with  $m_\pi$  and  $f_\pi$  being the pion mass and decay constant, respectively, and  $m_{u,d}$  are the up, down quark masses.

Below we will always assume the small  $\theta$  expansion. This is a crucial ingredient of our calculations, since it leads to a linear equation of motion. It is clear that our results will not include anharmonic effects when the field takes on values close to  $\theta \simeq \pm\pi$ . In the context of miniclusters those field values may lead to very dense objects [8, 9], which will not be contained in the mass function derived below and need to be considered as a correction to our results.

In the harmonic limit the equation of motion for the Fourier modes of the field decouple:

$$\ddot{\theta}_k + 3H(T)\dot{\theta}_k + \omega_k^2\theta_k = 0, \quad \omega_k^2 \equiv \frac{k^2}{a^2} + m(T)^2. \quad (2.5)$$

Qualitatively, we see that super-horizon modes with  $\omega_k \ll 3H$  are frozen,  $\theta_k = \text{const}$ , whereas they start to oscillate once they enter the horizon. We define  $T_{\text{osc}}$  as the temperature where the zero-mode (i.e., the homogeneous field) starts to oscillate by the equation

$$3H(T_{\text{osc}}) = m(T_{\text{osc}}). \quad (2.6)$$

The corresponding time and scale factors are denoted by  $t_{\text{osc}}$  and  $a_{\text{osc}}$ , respectively. Non-zero  $k$  modes will start to oscillate somewhat earlier. The redshifting of non-zero  $k$  modes is encoded by the  $1/a^2$  factor in the expression for  $\omega_k$  in eq. (2.5). For sufficiently late times the mass term will dominate for all modes and the energy density will behave like cold dark matter.

There are two main goals of this work:

Index	Description
$i$	time when we start the field evolution and set the initial conditions for the axion field correlator with the wave number scale $K \equiv a_i H_i$ , the default value is $T_i = 3T_{\text{osc}}$
osc	zero-mode starts to oscillate; defined by $3H(T_{\text{osc}}) = m(T_{\text{osc}})$
1	quantities at $T = 1$ GeV, with $K_1 \equiv a_1 H_1$ and $R_1 = 1/K_1$ used as reference scale for wave number or length-scale plots
$\star$	$T_\star \equiv 100$ MeV, axion mass reaches its zero-temperature value and all $k$ modes are non-relativistic; time when we start spherical collapse
eq	matter-radiation equality

**Table 1.** Summary of indices to denote quantities like time  $t$ , temperature  $T$ , Hubble rate  $H$ , and cosmic scale factor  $a$  at certain moments of evolution.

- Under the stated assumptions we calculate the energy density in the axion field based on the solutions of eq. (2.5), with initial conditions motivated by the post-inflation PQ breaking scenario. We derive an expression for the average axion energy density taking into account non-zero momentum modes. Furthermore we calculate the power spectrum of the density fluctuations which eventually will evolve into the miniclusters.
- In order to describe the subsequent evolution of the over-densities we consider a model of spherical collapse valid during both radiation and matter domination. Departing from the energy density power spectrum, we will apply a modified Press & Schechter formalism to estimate the mass and size of the gravitationally bound clumps of axion dark matter around the time of matter-radiation equality.

Our results will serve as input for the further evolution of the miniclusters. We do not address the question of how the minicluster evolves after it has decoupled from the Hubble flow. This is an important question which, however, is beyond the scope of this work.

For later reference we provide in table 1 a summary of indices that we use to denote certain points in the axion field and minicluster evolution.

### 3 Axion energy density and power spectrum

#### 3.1 Initial conditions

Let us specify our choice of initial conditions, which we impose shortly before the axion mass becomes important (we comment at the end of this subsection on our choice of the initial temperature). The axion field  $\theta(\vec{x})$  takes on random values in different Hubble patches. Therefore, we consider it as a random angular field with a flat probability distribution function  $f(\theta) = 1/(2\pi)$  for  $\theta \in [-\pi, \pi]$  and zero otherwise.<sup>1</sup> As usual, the expectation

<sup>1</sup>There is a subtlety related to this choice for  $f(\theta)$ , since being a random angular variable, any constant interval of length  $2\pi$  should be equivalent. Our choice is motivated by the fact that we adopt the harmonic approximation for the potential, which no longer is periodic. It turns out that in this case the flat distribution in the symmetric interval  $[-\pi, \pi]$  is the only physically meaningful choice. Any other interval would lead

value of any quantity  $Y(\theta)$  is given by  $\langle Y \rangle = \int d\theta f(\theta)Y(\theta)$ . In particular, it implies for the mean and the variance:

$$\langle \theta(\vec{x}) \rangle = 0, \quad \langle \theta(\vec{x})^2 \rangle = \pi^2/3. \quad (3.1)$$

Let us now consider the Fourier transform

$$\theta_k = \int_V d^3x \theta(\vec{x}) e^{i\vec{k}\vec{x}}, \quad \theta(\vec{x}) = \frac{1}{(2\pi)^3} \int d^3k \theta_k e^{-i\vec{k}\vec{x}}. \quad (3.2)$$

The integral over  $d^3x$  is taken over a large volume  $V$ , such that the integral is finite, and  $\vec{x}$  and  $\vec{k}$  are co-moving coordinate and momentum, respectively. We have  $\langle \theta_k \rangle = 0$ , and  $\theta_{-k} = \theta_k^*$  since  $\theta(\vec{x})$  is real. Due to statistical homogeneity and isotropy the correlation function in Fourier space can be written as

$$\langle \theta_k \theta_{k'}^* \rangle = (2\pi)^3 \delta^3(\vec{k} - \vec{k}') P_\theta(k), \quad (3.3)$$

where  $P_\theta(k)$  denotes the power spectrum for the field, which is the Fourier transform of the 2-point correlation function  $\xi(|\vec{r}|) = \langle \theta(\vec{x})\theta(\vec{x} + \vec{r}) \rangle$ . We follow the conventions for the power spectrum of Ref. [27].

We can now use the shape of the power spectrum to implement that causally disconnected regions should be uncorrelated. Let us introduce a characteristic wave number

$$K = a_i H_i, \quad (3.4)$$

where  $a_i$  is the scale factor at our initial time  $t_i$  and  $H_i$  is the Hubble rate at that time. The axion field should be uncorrelated at co-moving distances larger than  $1/K$ . Note that there is an ambiguity in this definition. Alternatively we could use the association of wave number and co-moving distance as  $k = \pi/R$ , which would lead to an additional factor  $\pi$  in eq. (3.4) for  $R = 1/(a_i H_i)$ . In general,  $K$  is defined only up to factors of order one, which unfortunately introduces a large uncertainty, since  $K$  enters in many quantities of interest with third power.

The normalization of the power spectrum is fixed by requiring  $\langle \theta(\vec{x})^2 \rangle = \pi^2/3$  according to eq. (3.1). The shape of the power spectrum should be determined by the evolution of the field from the PQ scale down to the QCD scale. In absence of a full simulation over so many orders of magnitude, we are forced to make some (physically motivated) guesses. A reasonable assumption seems to be a white noise (i.e., flat) power spectrum with a sharp cut-off at co-moving wave number  $K$  (“top-hat”):

$$P_\theta^{\text{TH}}(k) = \frac{2\pi^4}{K^3} \Theta(K - k). \quad (3.5)$$

This means that fluctuations for each mode up to  $K$  are equally likely. However, the finite cut-off leads to an oscillating two-point correlation function  $\xi(r)$  which decreases only with the inverse of the distance-squared, and hence, implies long-range correlations in

---

to unphysical implications of the zero mode.

configuration space beyond the horizon. Therefore we consider as alternative a Gaussian suppression of high wave numbers:

$$P_\theta^G(k) = \frac{8\pi^4}{3\sqrt{\pi}K^3} \exp\left(-\frac{k^2}{K^2}\right), \quad (3.6)$$

which leads to exponential suppression of correlations also in configuration space. Therefore, the Gaussian power spectrum seems to be physically better motivated and we adopt it as our default assumption. We will, however, also study the  $k$ -space top-hat power spectrum, since it provides a sharp cut-off to all the integrals in the following, making the effect of the scale  $K$  more transparent.

Equation (3.3) together with our assumptions on the power spectrum, eq. (3.6) respectively eq. (3.5), serve as initial condition for the field evolution which we consider in the following. Before proceeding let us comment on the choice of our initial time  $t_i$ , or the corresponding temperature  $T_i$ . We want to set  $T_i$  above the scale when the axion mass becomes important, in order to capture this process correctly by solving the equation of motion. On the other hand, we cannot set  $T_i$  much higher, since our formalism does not describe the effect of the topological strings, which are essential for describing the random massless field. Therefore, we chose to set  $T_i = 3T_{\text{osc}}$ , with  $T_{\text{osc}}$  determined by eq. (2.6). The actual value depends on the chosen axion mass, but typical values are  $T_{\text{osc}} \simeq 1$  GeV. Since this energy scale appears profusely in our calculations, we will present our results in units of the wavenumber  $K_1 = a_1 H_1$  or the co-moving distance  $R_1 = K_1^{-1}$ , where  $a_1$  and  $H_1$  are evaluated at the temperature of 1 GeV.

### 3.2 The average energy density

Sticking to the quadratic potential, the energy density of the axion field is given by

$$\rho(\vec{x}) = \frac{f_{\text{PQ}}^2}{2} \left[ \dot{\theta}^2 - \frac{1}{a^2} (\vec{\nabla}\theta)^2 + m^2(T) \theta^2 \right]. \quad (3.7)$$

Since the evolution equation is linear in the harmonic approximation, the Fourier modes evolve independent according to eq. (2.5) and we can write

$$\theta_k(a) = \theta_k f_k(a). \quad (3.8)$$

Here  $\theta_k \equiv \theta_k(a_i)$  denotes the initial condition for the field at the time  $t_i$  and  $f_k(a)$  is a real function encoding the time (or  $a$ ) dependence obtained from solving the equation of motion with the initial condition  $f_k(a_i) = 1$ . The random properties of the field characterized by Eq. (3.3) are thus encoded in the initial conditions  $\theta_k$ . We solve eq. (2.5) numerically for a large set of modes, for details see appendix A. We use the susceptibility  $\chi(T)$  as well as the effective number of degrees of freedom as a function of temperature needed to determine  $H(T)$  from the QCD calculations from Ref. [28], see also Refs. [29, 30] for similar calculations.

With this notation we obtain for the energy density

$$\rho(\vec{x}) = \frac{1}{(2\pi)^6} \frac{f_{\text{PQ}}^2}{2} \int d^3k d^3k' \theta_k \theta_{k'}^* F(k, k') e^{-i\vec{x}(\vec{k}-\vec{k}')}, \quad (3.9)$$

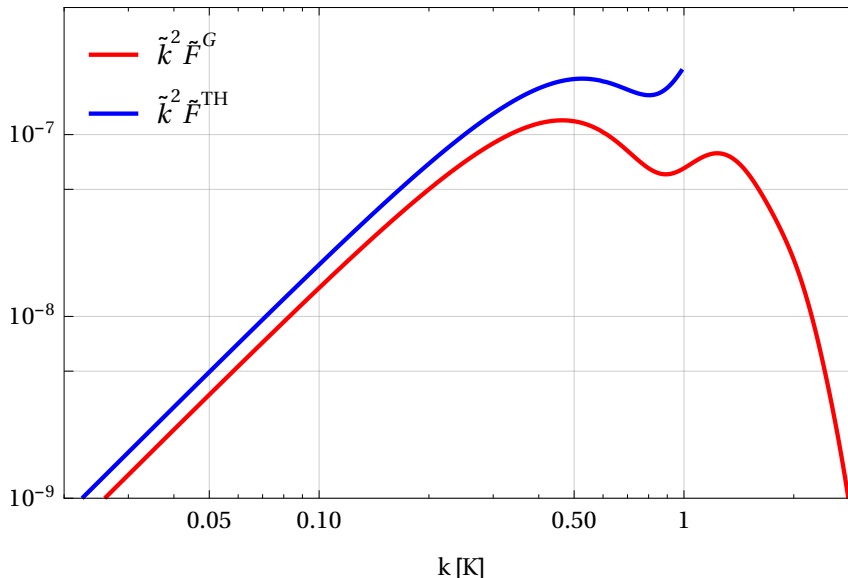


**Figure 1.** Contributions to the average energy density according to Eq. (3.13) when using the top-hat (TH) (blue) respectively the Gaussian (G) (red) power spectrum for the axion field. For the plot we chose  $f_{\text{PQ}} = 10^{12}$  GeV.

where we have defined

$$F(k, k') = \dot{f}_k \dot{f}_{k'} + \left( \frac{\vec{k} \cdot \vec{k}'}{a^2} + m^2(T) \right) f_k f_{k'}. \quad (3.10)$$

The average energy density is obtained by using the correlator from eq. (3.3) as

$$\bar{\rho} \equiv \langle \rho(\vec{x}) \rangle = \frac{1}{2\pi^2} \frac{f_{\text{PQ}}^2}{2} \int_0^\infty dk k^2 P_\theta(k) F(k, k), \quad (3.11)$$

with

$$F(k, k) = \dot{f}_k^2 + \omega_k^2 f_k^2, \quad (3.12)$$

where  $\omega_k$  has been defined in eq. (2.5) and it can be identified with the energy of the mode with momentum  $\vec{k}$ . Since the power spectrum suppresses modes with  $k > K$ , at sufficiently late times, the term  $k^2/a^2$  can be neglected compared to the zero-temperature mass  $m$ . We say that all modes become non-relativistic.

Let us introduce the dimensionless wave number  $\tilde{k} = k/K$ . It follows from the equation of motion that once all relevant modes have become non-relativistic and  $m(T)$  reached its zero-temperature value,  $F$ , and consequently  $\bar{\rho}$ , scales as  $a^{-3}$ , as it should for cold dark matter. We factor out the  $a^{-3}$  dependence and use  $m_0^2$  in order to define a dimensionless quantity  $\tilde{F}$  through  $F = m_0^2 (a_\star/a)^3 \tilde{F}$ , with  $a_\star$  corresponding to  $T_\star = 100$  MeV. Assuming for illustration the top-hat power spectrum defined in eq. (3.5), we find

$$\bar{\rho} = \frac{f_{\text{PQ}}^2}{2} m_0^2 \left( \frac{a_\star}{a} \right)^3 \pi^2 \int_0^1 d\tilde{k} \tilde{k}^2 \tilde{F}(\tilde{k}, \tilde{k}) \quad (P_\theta^{\text{TH}}). \quad (3.13)$$



We illustrate the contribution of the  $k$ -modes in fig. 1 for both the top-hat as well as the Gaussian correlator. While the former just cuts off modes with  $k > K$ , the latter provides a smooth suppression. Note that the combination  $f_{\text{PQ}}^2 m_0^2$  in eq. (3.13) is independent of  $f_{\text{PQ}}$ ; the  $f_{\text{PQ}}$  dependence is hidden in this expression in the function  $F(k, k)$ , whose shape and normalization depends on  $T_{\text{osc}}$  which in turn depends on  $f_{\text{PQ}}$ . Equation (3.13) agrees parametrically with the classical result, e.g. Refs. [31–34]:

$$\rho \sim f_{\text{PQ}}^2 m(a_{\text{osc}}) m_0 \left( \frac{a_{\text{osc}}}{a} \right)^3 \theta_{ini}^2, \quad (3.14)$$

where  $\theta_{ini}$  denotes some “initial” mis-alignment angle. The usual assumption in the post-inflation scenario,  $\theta_{ini}^2 = \pi^2/3$ , is replaced in our result by the proper weighted contribution of non-zero  $k$ -modes according to the initial power spectrum.

Numerically we find for the current energy density of the axions relative to the critical density due to the re-alignment mechanism in the stated approximations:

$$\Omega h^2 \approx 0.1 \left( \frac{f_{\text{PQ}}}{10^{12} \text{ GeV}} \right)^{7/6} \approx 0.1 \left( \frac{m_0}{5.7 \times 10^{-6} \text{ eV}} \right)^{-7/6}. \quad (3.15)$$

This is in good agreement with other recent results, for instance Refs. [35–37]. The numerical coefficient 0.1 depends somewhat on our assumptions. The energy density is about a factor 2 larger when we change the initial temperature from  $T_i = 3T_{\text{osc}}$  to  $T_i = 2T_{\text{osc}}$  because  $k$ -modes have less time to red-shift before they become non-relativistic. The dependence on the chosen field correlator (Gauss versus top-hat) is less than 30%. In the following we will show results for  $f_{\text{PQ}}$  equal to  $10^{10}$ ,  $10^{11}$  and  $10^{12}$  GeV, spanning approximately the range where the re-alignment mechanism provides 0.5% to 100% of the dark matter energy density.

### 3.3 Axion energy density power spectrum

In this subsection we will compute the power spectrum of the density contrast of the axion field. For the Fourier transform of the density we find

$$\rho_q = \frac{1}{(2\pi)^3} \frac{f_{\text{PQ}}^2}{2} \int d^3k \theta_k \theta_{k-q}^* F(k, k-q), \quad (3.16)$$

with  $\langle \rho_q \rangle \propto \delta^3(\vec{q})$  following from eq. (3.3). Now we consider the density contrast:

$$\delta(\vec{x}) \equiv \frac{\rho(\vec{x}) - \bar{\rho}}{\bar{\rho}}, \quad (3.17)$$

with its Fourier transform  $\delta_q = \rho_q / \bar{\rho}$  ( $q \neq 0$ ). The power spectrum is related to the variance of  $\delta_q$  by  $P(q) = \langle |\delta_q|^2 \rangle / V = \langle |\rho_q|^2 \rangle / (V \bar{\rho}^2)$ , see e.g., Ref. [27]. Hence, we calculate:

$$\langle |\rho_q|^2 \rangle = \left[ \frac{1}{(2\pi)^3} \frac{f_{\text{PQ}}^2}{2} \right]^2 \int d^3k d^3k' \langle \theta_k \theta_{k-q}^* \theta_{k'}^* \theta_{k'-q} \rangle F(k, k-q) F^*(k', k'-q). \quad (3.18)$$

With Wick's Theorem one obtains

$$\langle \theta_k \theta_{k-q}^* \theta_{k'}^* \theta_{k'-q} \rangle = \langle \theta_k \theta_{k-q}^* \rangle \langle \theta_{k'}^* \theta_{k'-q} \rangle + \langle \theta_k \theta_{k'}^* \rangle \langle \theta_{k-q}^* \theta_{k'-q} \rangle + \langle \theta_k \theta_{k'-q} \rangle \langle \theta_{k-q}^* \theta_{k'}^* \rangle \quad (3.19)$$

$$= (2\pi)^6 P_\theta(|\vec{k}|) P_\theta(|\vec{k} - \vec{q}|) \left\{ [\delta^3(\vec{k} - \vec{k}')]^2 + [\delta^3(\vec{k} + \vec{k}' - \vec{q})]^2 \right\}. \quad (3.20)$$

where we have used eq. (3.3) and we have dropped terms with  $\delta^3(\vec{q})$  by assuming  $q \neq 0$ . In order to deal with the squares of the Dirac delta function we use  $\delta^3(k=0) = V/(2\pi)^3$ . The first term in the curly bracket of eq. (3.20) gives  $|F(k, k-q)|^2$ . For the second term we can use that  $F(q-k, -k) = F(k, k-q)$ , which follows from  $f_k = f_{-k}^*$ . Hence the first and second terms are equal and we obtain

$$\langle |\rho_q|^2 \rangle = 2 \frac{V}{(2\pi)^3} \left( \frac{f_{\text{PQ}}^2}{2} \right)^2 \int d^3k P_\theta(|\vec{k}|) P_\theta(|\vec{k} - \vec{q}|) F(k, k-q)^2 \quad (3.21)$$

Using eq. (3.11) for  $\bar{\rho}$  this gives for the power spectrum

$$P(q) = \frac{1}{V} \frac{\langle |\rho_q|^2 \rangle}{\bar{\rho}^2} = 2(2\pi)^3 \frac{\int d^3k P_\theta(|\vec{k}|) P_\theta(|\vec{k} - \vec{q}|) F(k, k-q)^2}{[\int d^3k P_\theta(k) F(k, k)]^2}. \quad (3.22)$$

The function  $F(k, k')$  defined in eq. (3.10) is obtained from solving the equation of motion as described in appendix A and it depends on time. Once the axion has reached its zero-temperature mass and all relativistic modes have been red-shifted away,  $F(k, k')$  scales as  $a^{-3}$ , independent of  $k, k'$ . Hence the time dependence in numerator and denominator of eq. (3.22) cancels and the power spectrum becomes constant in time. Our numerical calculation shows that for temperatures below

$$T_\star \equiv 100 \text{ MeV} \quad (3.23)$$

this is indeed the case. Since for the following considerations we only need the power spectrum, we can stop the field evolution at that point. In the left panel of fig. 2 we plot the power spectrum at  $T_\star$  for different choices of  $f_{\text{PQ}}$ . We observe constant power at small  $q$  (large scales), corresponding to white noise. Then the power drops at a characteristic scale, corresponding roughly to the size of the miniclusters, and is suppressed for large wave numbers (small scales) where fluctuations are erased by the gradient terms.

In the right panel of fig. 2 we show the dimensionless power spectrum

$$\Delta^2(q) = \frac{q^3}{2\pi^2} P(q), \quad (3.24)$$

which corresponds to the variance of the relative density perturbations per decade of  $q$ . From the plot we see that relative density fluctuations are of order one, i.e., non-linear. Furthermore, the peak in the relative density fluctuations is at a characteristic wave number corresponding to a scale a few times smaller than the horizon at  $T_{\text{osc}}$ . This can be seen for instance by considering the orange curve, corresponding to  $f_{\text{PQ}} = 10^{12}$  GeV. For this case,  $T_{\text{osc}} \approx 1$  GeV, and hence  $K_1 = a_1 H_1$  is the inverse of the horizon at  $T_{\text{osc}}$ . The peak for the orange curve is around  $q \approx 4K_1$ , and hence it corresponds to a size 4 times smaller than

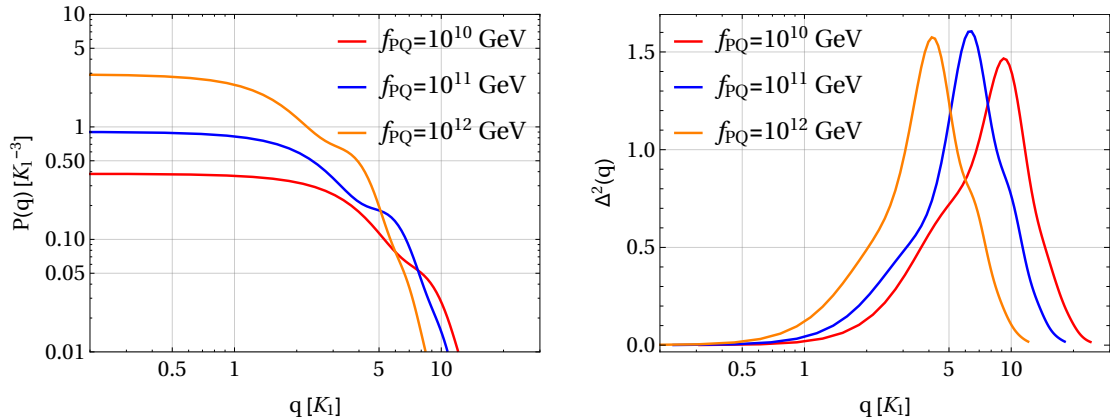


**Figure 2.** The axion energy density power spectrum  $P(q)$  (left) and the dimensionless power spectrum  $\Delta^2(q)$  defined in eq. (3.24) (right), for different choices of  $f_{\text{PQ}}$ , assuming the Gaussian initial axion field correlator. As reference scale we use the comoving wave number at 1 GeV:  $K_1 = a_1 H_1$ .

the horizon at  $T_{\text{osc}}$ . For the other two curves,  $f_{\text{PQ}}$  is smaller, which means larger  $T_{\text{osc}}$ , and therefore the peak is shifted to smaller length scales accordingly.

In fig. 3 we show the impact of our initial assumptions on  $\Delta^2(q)$ . An interesting result is that the power spectrum has a cut-off around  $2K$  (instead of the naively expected  $K$ ). This is most transparent for the case when we consider a top-hat initial correlator for the axion field according to eq. (3.5), where we have a sharp cut-off in  $k$ -space. For  $f_{\text{PQ}} = 10^{12}$  GeV we have  $K/K_1 = a_i H_i / (a_1 H_1) \approx a_1 / a_i \approx 3$ , since  $T_i / (1 \text{ GeV}) \approx T_i / T_{\text{osc}} = 3$ . Therefore, the value  $q/K_1 \approx 6$ , at which the dash-dotted curve in the left panel of fig. 3 goes to zero corresponds to  $2K$ . This result follows directly from the way how the two  $P_\theta$  factors in eq. (3.22) depend on the wave number, and it implies that although modes with  $k > K$  do not contribute to the energy density, there is power in fluctuations up to wave numbers  $2K$ . Note that for the Gaussian correlator, eq. (3.6), which is our default assumption, the cut-off is smeared out.

The comparison of the solid and dashed curves in the right panel of fig. 3 shows the effect of changing our default assumption  $T_i = 3T_{\text{osc}}$  to  $T_i = 2T_{\text{osc}}$ . Note that this implies also a change of the wave number cut-off, which we define as  $K = a_i H_i$ . As expected we observe a shift of the peak towards smaller wave numbers.

A note on the normalization of our power spectrum is in order. We use  $\bar{\rho}$  to normalize the spectrum, which is the average density from the re-alignment mechanism. If there is an additional contribution to the axion energy density (e.g., from the string and domain wall decay) the power would be reduced accordingly, unless the additional component itself introduces further fluctuations.

Our calculations so-far do not include the effect of gravity on the axion over-densities, therefore the expression for the power spectrum, eq. (3.22) remains constant after  $T_\star$ . In the following we are going to “switch on” gravity for the axions, and develop a model to

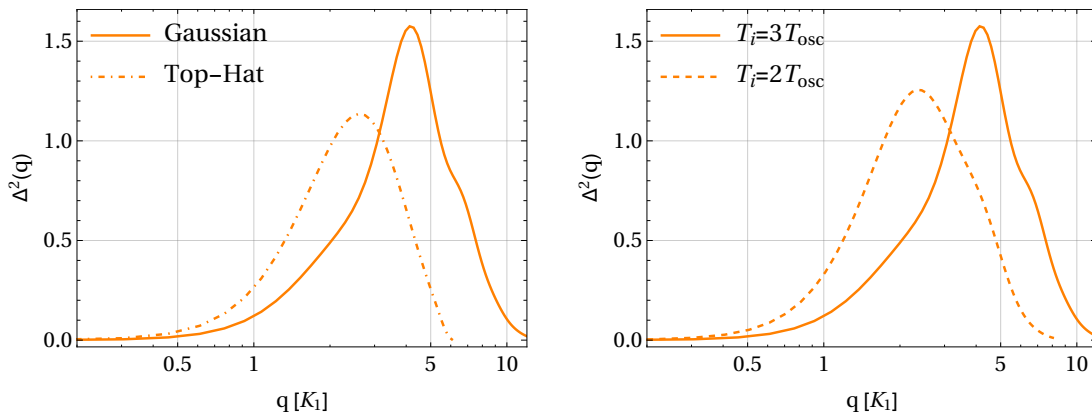


**Figure 3.** The dimensionless power spectrum  $\Delta^2(q)$  for  $f_{\text{PQ}} = 10^{12}$  GeV. In the left panel we compare  $\Delta^2(q)$  for the different initial field correlators, Gaussian (G) and top-hat (TH), as defined in eq. (3.6) respectively eq. (3.5). The right panel shows  $\Delta^2(q)$  assuming different initial times  $T_i$ , when using the same correlator (G). The reference scale,  $K_1 = a_1 H_1$ , is the comoving wave number at 1 GeV. The solid curve in both panels corresponds to our default assumption,  $T_i = 3T_{\text{osc}}$  and Gaussian correlator, and is the same as the orange solid curve in the right panel of fig. 2.

describe the over-densities up to the point when they decouple from the Hubble expansion. The power spectrum at  $T_\star$  discussed in this section will be the input for those calculations.

#### 4 The size and mass of axion miniclusters

In standard cold dark matter cosmology, the Press & Schechter [38] (PS) method and its variants are useful tools to estimate the mass function of gravitationally collapsed objects (for reviews see e.g., Refs. [27, 39]). The basic idea is to use a spherical collapse model for an over-density to estimate a critical density contrast,  $\delta_c$ , such that regions with  $\delta > \delta_c$  are collapsed. PS provide a rule to use this result to estimate the mass function,  $dn/dM$ , which is the number density of collapsed objects with mass in the interval  $[M, M + dM]$ . Below we provide a modification of the standard method to take into account several peculiarities of the small-scale fluctuations in the axion energy density:

1. As is clear from the previous section, density fluctuations are of order one from the initial moment when they are created. Therefore, linear theory cannot be used.
2. The non-linear fluctuations are created around  $T \sim 1$  GeV, deep inside the radiation dominated era. We need a collapse model which is valid both during radiation and matter domination.
3. We will be interested in the double differential mass function  $dn/dMdR$ , providing the density of objects with a certain mass and a certain size. We develop a modified PS approach to calculate  $dn/dMdR$ , taking again into account the non-linearity of the fluctuations.

In sections 4.1 and 4.2 we present the spherical collapse model and our derivation of the double differential mass function under those requirements, with the main result for  $dn/dMdR$  given in eq. (4.14). The reader mostly interested in the application of that result to axions may directly skip to section 4.3, where we present the results of our calculation for the minicluster distribution around matter-radiation equality.

#### 4.1 Spherical collapse model

Kolb & Tkachev (KT) [40] provide a method to describe spherical collapse during and after radiation domination. Here we do not repeat their calculation but just present briefly the approach and state the results, which we are going to apply in the following. The equation of motion for a spherical shell of matter, including a homogeneous radiation background energy density,  $\rho_{\text{rad}}$ , is described by the differential equation

$$\ddot{r} = -\frac{8\pi G}{3}\rho_{\text{rad}}r - \frac{GM}{r^2}, \quad (4.1)$$

where  $r$  is the physical radius and the total dark matter mass  $M$  enclosed in the sphere of radius  $r$  is assumed to remain constant during collapse. Let us denote by  $r_{\text{flow}}$  the physical coordinate describing the background expansion. Then we introduce the dimensionless variable  $\xi$  to describe the deviation of the over-density from this expansion:  $r = \xi r_{\text{flow}}$ . KT derived an equation of motion for  $\xi$ :

$$x(1+x)\frac{d^2\xi}{dx^2} + \left(1 + \frac{3}{2}x\right)\frac{d\xi}{dx} + \frac{1}{2}\left(\frac{1+\delta}{\xi^2} - \xi\right) = 0, \quad (4.2)$$

where  $x \equiv a/a_{\text{eq}}$ , with  $a_{\text{eq}}$  being the scale factor at matter-radiation equality. The density contrast  $\delta$  is the over-density at the initial time where we start the evolution. It is related to  $M$  through

$$M = \frac{4\pi}{3}\bar{\rho}(1+\delta)r^3, \quad (4.3)$$

with  $r$  denoting the initial size of the over-dense region. Eq. (4.2) is valid both in the radiation and matter domination era. The solution  $\xi(x)$  of eq. (4.2) can be used to identify the time when an over-density collapses by requiring  $\dot{r} = 0$ , i.e., when the over-density “turns around” and starts to contract. We have verified by numerically solving eq. (4.2) the result of KT, namely that an initial over-density  $\delta$  at an early time will turn around at  $x$  if  $\delta > \delta_c$  with

$$\delta_c(x) \approx \frac{0.7}{x}. \quad (4.4)$$

This result holds for  $x < 1$  (radiation domination) as well as  $x > 1$  (matter domination), and is to good approximation independent of the initial time. As we have seen above, the minicluster power spectrum remains constant shortly after all modes became non-relativistic and the axion reaches its zero-temperature mass. Hence, the precise point when we start the spherical collapse is not important as long as the corresponding temperature is less than  $T_\star = 100$  MeV. For definiteness, we set the initial time of the collapse calculation to that temperature and denote initial quantities with the index  $\star$ .

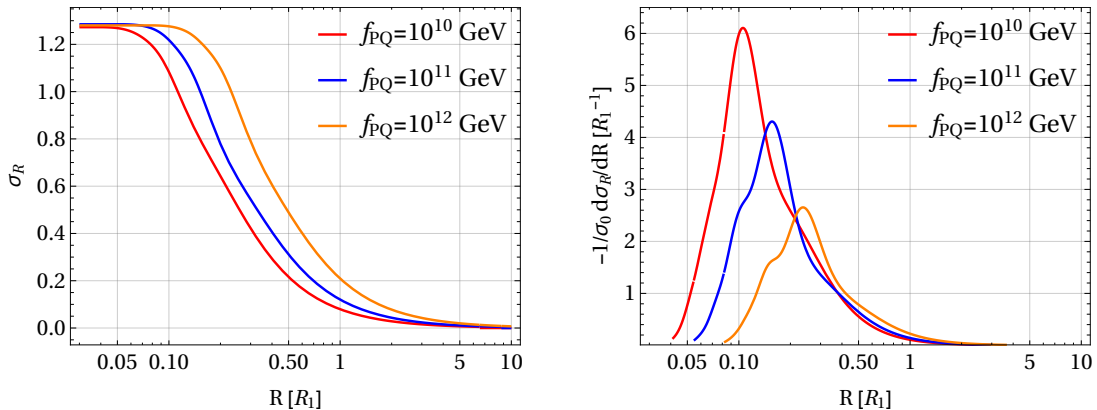


**Figure 4.** Standard deviation of the smoothed density field (left) and relative derivative of the standard deviation,  $-1/\sigma_0 d\sigma_R/dR$ , (right) as a function of the smoothing scale  $R$  for different choices of  $f_{\text{PQ}}$ . The reference length scale is the co-moving size of the horizon at 1 GeV:  $R_1 = 1/(a_1 H_1)$ .

## 4.2 Double differential mass function

Let us consider the axion energy density contrast smoothed over a characteristic length scale  $R$ :

$$\delta_R(\vec{x}) = \int d^3x' W_R(\vec{x} - \vec{x}') \delta(\vec{x}'), \quad (4.5)$$

where  $W_R(\vec{x})$  is a filter function which goes to zero if  $x \gg R$ . Then the variance of the smoothed density contrast is determined by the power spectrum:

$$\sigma_R^2 \equiv \langle \delta_R(\vec{x})^2 \rangle = \frac{1}{2\pi^2} \int_0^\infty dk k^2 P(k) \left| \tilde{W}_R(k) \right|^2, \quad (4.6)$$

where  $\tilde{W}_R(k)$  is the Fourier transform of the window function. We adopt a top-hat window function in  $k$  space:  $\tilde{W}_R(k) = \Theta(1 - kR)$ . We comment on the reason for this choice below. As visible in fig. 4,  $\sigma_R$  has a step-like shape with the characteristic scale ranging from 3 to 10 times smaller than the horizon at  $T = 1$  GeV, depending on the value of  $f_{\text{PQ}}$ .

We are going to assume that  $\delta_R(\vec{x})$  is a random Gaussian variable with variance  $\sigma_R^2$ , i.e., the probability to find a fluctuation in the smoothed energy density in the interval  $[\delta, \delta + d\delta]$  is

$$f_{\text{sm}}(\delta; R) = \frac{1}{\sqrt{2\pi}\sigma_R} \exp\left(-\frac{\delta^2}{2\sigma_R^2}\right). \quad (4.7)$$

Since  $\sigma_R$  is of order unity, large fluctuations are likely. The Gaussian shape implies then, that the total density can become negative. However, below we will be interested only in upward fluctuations  $\delta > 0$ , and therefore we are not applying eq. (4.7) in the potentially unphysical region. Furthermore, the Gaussian assumption for the fluctuations is consistent with using the harmonic potential. Large over-densities due to anharmonic effects may also lead to non-Gaussian tails of the distribution.

In the standard PS formalism a one-to-one correspondence between the smoothing scale  $R$  and the mass contained in the over-density is assumed by the ansatz  $M_R = V_R \bar{\rho}$ , with  $V_R$  being the volume associated with the window function. Here we want to relax this ansatz and allow for the fact that the variance of  $\delta$  is large. Therefore, the mass of an over-dense region depends both on the size  $r$  and the over-density  $\delta$  via eq. (4.3).

Our goal is now, departing from eq. (4.7), to derive the joint probability distribution function (pdf)  $f(\delta, r)$  for  $\delta$  and  $r$ , which gives the probability to find a fluctuation with  $\delta \in [\delta, \delta + d\delta]$  which has a size  $r \in [r, r + dr]$ . Note that eq. (4.7) is a pdf for  $\delta$  at fixed  $R$ , normalized to 1 for any  $R$ . The smoothing at scale  $R$  implies that only fluctuations with  $r > R$  can contribute to the pdf of  $\delta$ . Hence we make the ansatz

$$g(R) f_{\text{sm}}(\delta; R) = \int_R^\infty dr f(\delta, r), \quad (4.8)$$

where the function  $g(R)$  is introduced such that the marginal distribution  $f(r) \equiv \int d\delta f(\delta, r)$  is properly normalized:

$$g(R) = \int_R^\infty dr f(r), \quad g(0) = 1. \quad (4.9)$$

In general this leads to complicated integro-differential equations for the unknown functions  $g(r)$  and  $f(\delta, r)$ . However, using the Gaussian for  $f_{\text{sm}}(\delta; R)$  from eq. (4.7) we can try to guess the solution. By differentiating eq. (4.8) one obtains

$$f_{\text{sm}}(\delta; R) \left[ g'(R) - \frac{d \log \sigma_R}{dR} \left( 1 - \frac{\delta^2}{\sigma_R^2} \right) g(R) \right] = -f(\delta, R) \quad (4.10)$$

Indeed, it is easy to show that  $g(R) = \sigma_R/\sigma_0$  provides a solution, with  $\sigma_0 \equiv \sigma_{R=0}$  being the variance without smooting. Using eq. (4.10) we obtain:

$$f(\delta, R) = -\frac{1}{\sigma_0} \frac{d\sigma_R}{dR} \frac{\delta^2}{\sigma_R^2} f_{\text{sm}}(\delta; R), \quad (4.11)$$

$$f(R) = -\frac{1}{\sigma_0} \frac{d\sigma_R}{dR}. \quad (4.12)$$

The result for the marginal distribution in eq. (4.12) has an intuitive interpretation: the distribution of the size of the fluctuations is related to the change in the smoothing scale, and if  $\sigma_R$  is constant at a given scale  $R$ , there are no fluctuations of size  $r = R$  at that scale. We show some numerical examples of  $f(R)$  for the axion miniclusters in fig. 4.

Combining our result for  $f(\delta, r)$  with eq. (4.4), we can now proceed in analogy to the PS formalism and estimate the double differential mass function. We use that for fixed  $r$ , eq. (4.3) relates the mass  $M$  to the over-density  $\delta$ . We denote by  $dn/dMdR$  the comoving number density of collapsed objects with mass in  $[M, M + dM]$  and size in  $[R, R + dR]$ . It is related to  $f(\delta, r)$  by

$$\frac{M}{\bar{\rho}} \frac{dn}{dMdR} dMdR = 2 f(\delta, R) d\delta dR \Theta[\delta - \delta_c(x)]. \quad (4.13)$$

The theta-function selects over-densities larger than  $\delta_c(x)$ , which are collapsed at the time  $x$ . The factor of 2 is included here for the same reason as it appears in the original PS formula. It takes into account the mass in under-dense regions; if all mass was bound in collapsed objects (meaning  $\delta_c = 0$ ) the integral of the right-hand side of eq. (4.13) should give 1, whereas without the factor 2 it would give only 1/2. Using eq. (4.3) we obtain our final result for the double differential mass function:

$$\frac{dn}{dM dR} = \frac{3}{2\pi M R^3} f(\delta, R) \Theta[\delta - \delta_c(x)], \quad (4.14)$$

where  $f(\delta, R)$  is given in eq. (4.11),  $\delta$  is considered as a function of  $M$  and  $R$ ,  $\delta = \delta(M, R)$  according to eq. (4.3), and the critical density  $\delta_c(x)$  is given in eq. (4.4). The interpretation of eq. (4.14) is as follows:  $dn/dM dR$  is the distribution of collapsed objects at a time  $x = a/a_{\text{eq}}$ , whereas  $f(\delta, R)$  is the distribution of the fluctuations at the initial time  $x_*$ , which can be calculated departing from the power spectrum at  $x_*$  using eq. (4.11). The total mass function  $dn/dM$  is obtained by integrating over  $R$

$$\frac{dn}{dM} = \frac{3}{2\pi M} \int_0^{R_c(M)} \frac{dR}{R^3} f[\delta(M, R), R], \quad (4.15)$$

where  $R_c$  for a given  $M$  can be derived from eq. (4.3) with  $\delta = \delta_c(x)$ .

Before applying this result to the axion minicluster, let us come back to the question of how to choose the window function for smoothing the energy density. Since the minicluster power spectrum has a high-momentum cut-off, we do not expect to find structures at very small scales. In the mass function this is reflected by the proportionality to  $d\sigma_R/dR$  via eq. (4.11). Indeed, from fig. 4 we observe that  $d\sigma_R/dR$  goes to zero for small  $R$ . However, from eq. (4.14) we see that  $d\sigma_R/dR$  needs to go sufficiently fast to zero for  $R \rightarrow 0$  to compensate the factor  $1/(MR^3)$ . It turns out that both for a Gaussian, as well as a real-space top-hat window function, the mass function diverges for small  $M$  and  $R$ . Only the  $k$ -space top-hat indeed cuts off the small structures, since  $d\sigma_R/dR$  is exactly zero for  $1/R$  larger than the cut-off in the power spectrum. This is a well known problem also for the standard PS method, see, e.g., Ref. [16] for a recent discussion and further references. Therefore, we use the  $k$ -space top-hat smoothing function, which seems suitable to describe the physics of the power spectrum cut-off.

### 4.3 Minicluster mass and size distribution

In order to display our results for the axion minicluster mass function we introduce the dimensionless distributions

$$X_{MR} = \frac{M}{\bar{\rho}} \frac{dn}{d \log M d \log R} \quad (4.16)$$

and

$$X_M = \frac{M}{\bar{\rho}} \frac{dn}{d \log M}. \quad (4.17)$$



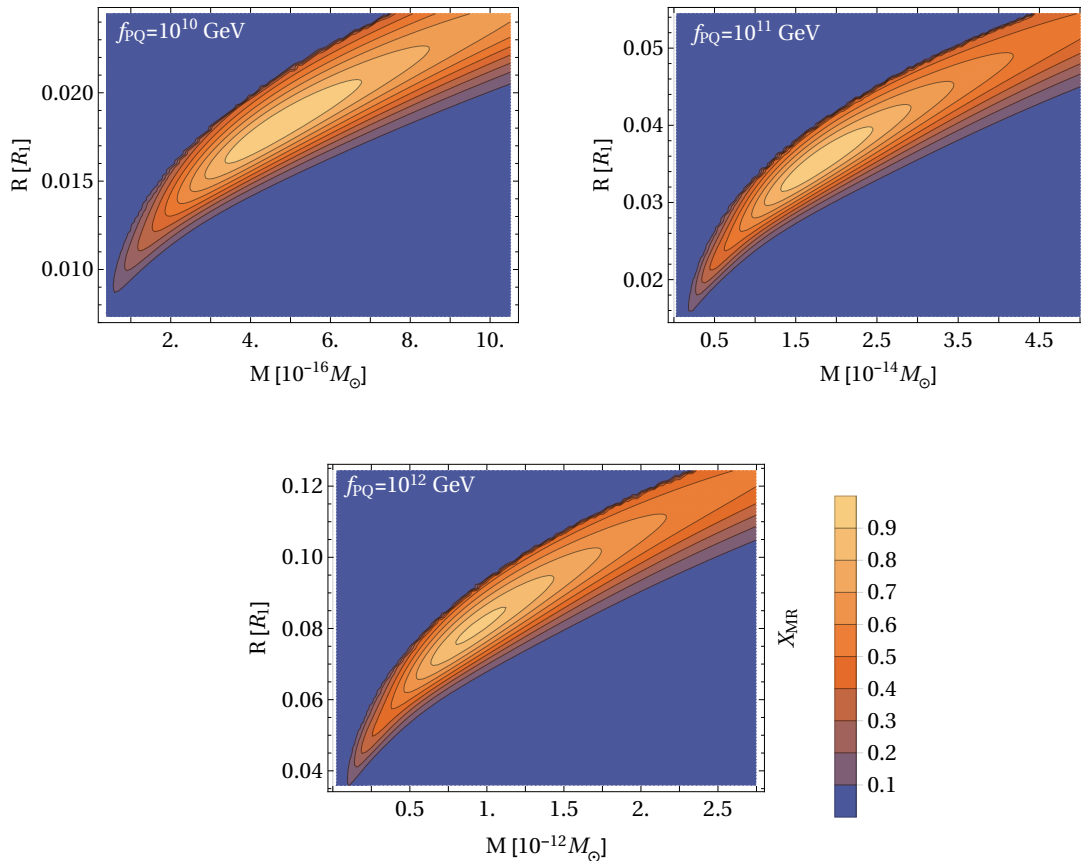


**Figure 5.** Dimensionless double differential distribution of collapsed objects  $X_{MR} \equiv M^2 R / \bar{\rho} (dn/dM dR)$  at matter-radiation equality for three choices of  $f_{PQ}$ . The vertical axis shows the co-moving size of the over-density at the initial time  $T_* = 100$  MeV relative to  $R_1$ , the co-moving Hubble radius at 1 GeV.

They correspond to the contribution of objects per decade in  $M$  and  $R$  for  $X_{MR}$  and only in  $M$  for  $X_M$ , relative to  $\bar{\rho}$ . Note that  $\bar{\rho}$  is the average energy density from the re-alignment mechanism as obtained in eq. (3.11), which in general will be smaller than the total energy density in axions due to the string and domain wall decay contribution. Hence, the possible presence of an additional energy density component will affect the normalization of the mass function as well as the power spectrum (and therefore  $\sigma_R$ ). Below we will focus mostly on the shape of our distributions. In fig. 5 we show the double differential distribution in  $M$  and  $R$  of collapsed miniclusters for three choices of  $f_{PQ}$ . We observe a peaked distribution with a clear correlation between mass and size of the objects.

In fig. 6 we show the  $R$ -integrated mass function. At matter-radiation equality (solid curves) we can make the following observations: the location of the peak of the distributions depends sensitively on  $f_{PQ}$ , ranging from  $10^{-16}$  to  $10^{-12} M_\odot$ . For given  $f_{PQ}$ , the range of masses which contribute more than 1% of the peak mass spans an interval of more than two orders of magnitude in  $M$  around the peak value, see table 2 for the numbers.

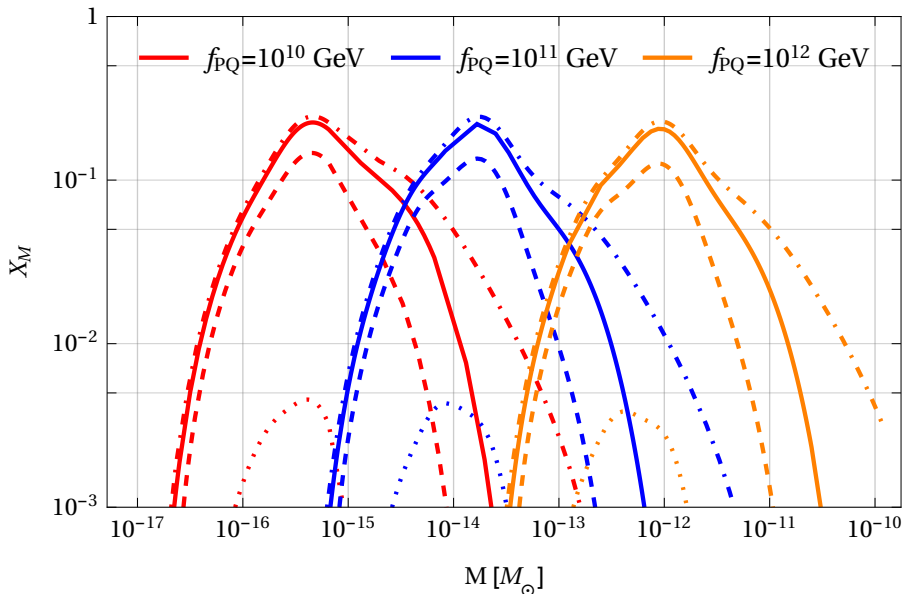


**Figure 6.** Dimensionless minicluster mass function  $X_M \equiv M^2/\bar{\rho}(dn/dM)$  for three choices of  $f_{\text{PQ}}$ . The different line-styles indicate the mass function at different times: dotted  $x = 0.2$ , dashed  $x = 0.5$ , solid  $x = 1$ , dot-dashed  $x = 5$ , where  $x = a/a_{\text{eq}}$ .

$f_{\text{PQ}}$ [GeV]	$M_{\text{peak}}$ [ $M_{\odot}$ ]	$M$ range [ $M_{\odot}$ ]	$r_{\text{ta}}^{\text{peak}}$ [km]	$r_{\text{ta}}$ range [km]
$10^{10}$	$4 \times 10^{-16}$	$[2 \times 10^{-17}, 1 \times 10^{-14}]$	$4 \times 10^4$	$[2 \times 10^4, 2 \times 10^5]$
$10^{11}$	$2 \times 10^{-14}$	$[5 \times 10^{-16}, 3 \times 10^{-13}]$	$2 \times 10^5$	$[4 \times 10^4, 7 \times 10^5]$
$10^{12}$	$8 \times 10^{-13}$	$[6 \times 10^{-14}, 2 \times 10^{-11}]$	$2 \times 10^6$	$[7 \times 10^5, 7 \times 10^6]$

**Table 2.** For three example values of  $f_{\text{PQ}}$  we give the minicluster mass for which the relative mass function  $X_M$  peaks,  $M_{\text{peak}}$ , and the interval in masses, where the mass function  $X_M$  is larger than 1% of the peak. The column “ $r_{\text{ta}}^{\text{peak}}$ ” gives the size of the over-density corresponding to  $M_{\text{peak}}$  when it decouples from the Hubble flow and starts to collapse (“turn-around”). The last column gives the range of  $r_{\text{ta}}$  corresponding to masses for which the mass function  $X_M$  is larger than 1% of the peak.

The different line-styles in fig. 6 show the mass function at different times around matter-radiation equality, ranging from  $x = 0.2$  till  $x = 5$ . Note that with the normalization of the distribution according to eq. (4.17) the expansion effect is factored out and the plot shows the change of the number of objects per co-moving volume. We find that the collapse process largely finishes at matter-radiation equality ( $x = 1$ , solid curves). For late times we see some hierarchical collapsing at the high mass end. But we checked that the dash-dotted curves ( $x = 5$ ) are already close to the  $x \rightarrow \infty$  limit. This can be understood from the analytic expression, eq. (4.15), in the limit  $\delta_c \rightarrow 0$ .

Estimates of the minicluster mass in the previous literature assume that a minicluster is made out of all axions inside the Hubble horizon  $d_H$  at the time the field oscillations commence [7]:  $M \sim \frac{4\pi}{3} d_H^3(T_{\text{osc}})\bar{\rho}(T_{\text{osc}})$ . Using  $d_H \sim 1/H$ , this leads to (see e.g., Refs. [12,

17, 18])  $M \sim 10^{-12} M_\odot (f_{\text{PQ}}/10^{11} \text{ GeV})^2$ . While our results show a similar dependence on  $f_{\text{PQ}}$ , the values for  $M_{\text{peak}}$  obtained from fig. 6 are about two orders of magnitude smaller. This follows from the fact that the characteristic size of the density fluctuations is smaller than the Hubble horizon at  $T_{\text{osc}}$ . Let us consider the horizon in co-moving coordinates,  $d_H/a = 1/(aH)$ , at  $T_{\text{osc}}$  relative to our reference scale  $R_1$ :

$$\frac{d_H(T_{\text{osc}})}{a_{\text{osc}}} \frac{1}{R_1} = \frac{a_1 H_1}{a_{\text{osc}} H_{\text{osc}}} = [0.49, 0.66, 1] \quad \text{for } f_{\text{PQ}} = [10^{10}, 10^{11}, 10^{12}] \text{ GeV}. \quad (4.18)$$

Considering figs. 4 and 5, those numbers imply that the typical scale of the miniclusters is smaller than the size of the horizon at  $T_{\text{osc}}$  and therefore we obtain lighter miniclusters. Note that Ref. [15] obtains an even larger minicluster mass, since their definition of the ‘‘Hubble volume’’ differs by a factor  $\pi$  from the above estimate  $d_H \sim 1/H$ .

Let us now discuss the size of the miniclusters. The quantity shown on the vertical axes of fig. 5 is not very intuitive: it corresponds to the co-moving size of the over-density at the initial time  $T_\star = 100 \text{ MeV}$  relative to the co-moving Hubble radius at 1 GeV. In order to convert this into a more useful quantity, we calculate now the physical size of an over-density of given mass, at the time when it decouples from the Hubble flow, i.e., at turn-around, denoted by  $r_{\text{ta}}$ . In the notation of section 4.1, it is given by

$$r_{\text{ta}} = \xi_{\text{ta}} a_{\text{ta}} R, \quad (4.19)$$

where  $R$  is the initial co-moving radius. By using eq. (4.3) and solving eq. (4.2) numerically one can get  $\xi_{\text{ta}}$  and  $a_{\text{ta}}$ . An approximate analytic expression can be obtained by using [40]  $\xi \simeq 1 - \delta x/2$ , together with  $\delta x_{\text{ta}} \simeq 0.7$ . Introducing a minor fudge factor to fit numerics we find

$$r_{\text{ta}} \simeq 0.4 \frac{R a_{\text{eq}}}{\delta} = 0.4 \frac{a_{\text{eq}}}{a_1 H_1} \frac{(R/R_1)^4}{M/M_1 - (R/R_1)^3} \quad (4.20)$$

where in the last step we use eq. (4.3) to express  $\delta$  in terms of  $R$ ,  $M$  and a reference mass at  $T_1 = 1 \text{ GeV}$  defined as  $M_1 \equiv \frac{4\pi}{3} \bar{\rho}_1 H_1^{-3}$ . Equation (4.20) makes clear that a higher initial over-density leads to earlier collapse and thus a smaller physical radius, compared to objects which are less dense and therefore need a longer collapse time. In the parameter range relevant for axion miniclusters, we find that the  $M/M_1$  term in the denominator of eq. (4.20) is a factor of  $10^2$  larger than the  $(R/R_1)^3$  term. Neglecting the latter then allows us to write  $r_{\text{ta}}$  as

$$r_{\text{ta}} \simeq 1.4 \times 10^9 \text{ km} \left( \frac{R}{R_1} \right)^4 \left( \frac{M_1}{M} \right), \quad (4.21)$$

where we have used  $T_{\text{eq}} = 0.8 \text{ eV}$ .  $M_1$  depends on  $f_{\text{PQ}}$  via  $\bar{\rho}$ . For our three example values we obtain

$$r_{\text{ta}} \simeq [2, 25, 360] \times 10^{10} \text{ km} \left( \frac{R}{R_1} \right)^4 \left( \frac{10^{-14} M_\odot}{M} \right), \quad f_{\text{PQ}} = [10^{10}, 10^{11}, 10^{12}] \text{ GeV}. \quad (4.22)$$

Those estimates are in good agreement with the numerical results for  $r_{\text{ta}}$ , which are shown in the upper panel of fig. 7. We show the relationship between  $R$  and  $r_{\text{ta}}$  for different

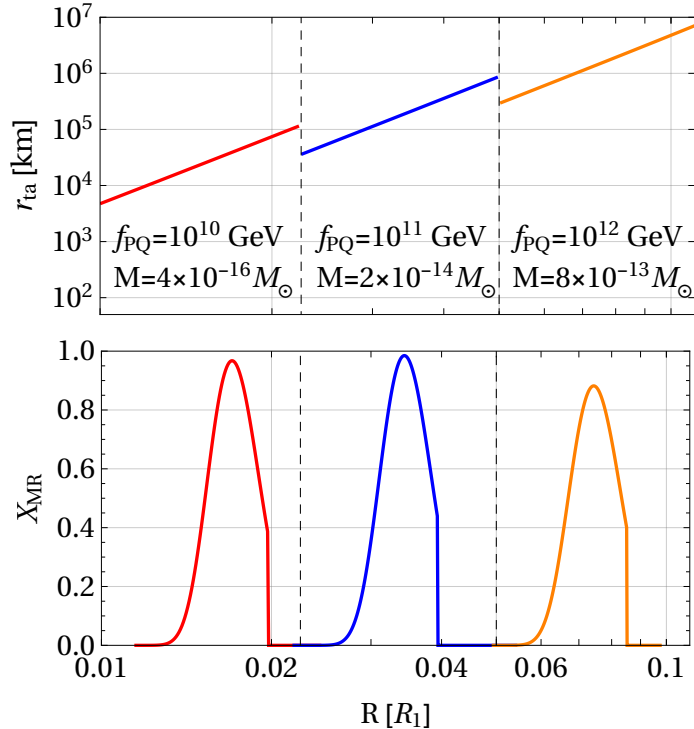


**Figure 7.** *Upper panel:* The physical radius of an over-density with mass  $M$  at the time when it decouples from the Hubble flow, as a function of its initial comoving size  $R$ , cf. eq. (4.20). The masses are chosen such that they correspond to the peak values of the minicluster mass function, cf. table 2. *Lower panel:* Slices through the dimensionless distribution function  $X_{MR}$ , defined in eq. (4.16), for constant  $M$ . Again the masses are fixed to the peak values of  $X_{MR}$ , as in the upper panel. For both panels the reference scale is the co-moving horizon size at 1 GeV,  $R_1$ .

characteristic masses, corresponding to our three choices of  $f_{\text{PQ}}$ . The abundance of objects of the corresponding masses can be seen in the lower panel, where we give slices through the 2-dimensional distributions at the corresponding values of  $M$ . At the peaks of the distributions shown in the lower panel we find physical sizes at turn around of  $3.9 \times 10^4$ ,  $1.9 \times 10^5$  and  $1.5 \times 10^6$  km. In table 2 we give also the interval in  $r_{\text{ta}}$  corresponding to the masses for which the mass function  $X_M$  is larger than 1% of its maximum. For given  $f_{\text{PQ}}$  the sizes of the miniclusters at turn-around span approximately one order of magnitude.

## 5 Discussion and Summary

In this paper we have developed a semi-analytic method to estimate the distribution of axion miniclusters from the re-alignment mechanism. Starting from an assumption on the statistical properties of the axion field shortly before the QCD phase transition, we calculate the resulting energy density power spectrum at the point when all axions have become non-relativistic and the zero-temperature axion mass is recovered, which happens around a temperature of 100 MeV. Departing from the power spectrum we use a spherical

collapse model and a modified Press & Schechter approach to obtain the distribution of gravitationally bound miniclusters in mass and size at the point when they decouple from the Hubble flow and start to collapse gravitationally. We find that for a given PQ breaking scale, the masses of miniclusters contributing relevantly to the energy density span more than two orders of magnitude, with peak values which are about two orders of magnitude smaller than obtained from naive estimates.

## 5.1 Adopted assumptions and limitations

Let us re-state here our most important assumptions and point out the limitations of our approach.

1. *Initial power spectrum of the axion field.* As our initial condition we assume statistical properties of the axion field before the QCD phase transition, motivated by the physics that field values in causally disconnected regions at that time should be uncorrelated. This is implemented in terms of the initial field power spectrum  $P_\theta(q)$ , and our default assumption is a Gaussian correlator with a characteristic scale set by the horizon at temperatures of a few GeV, see eqs. (3.3), (3.4) and (3.6). In a more realistic approach, this power spectrum should be determined from the non-linear field evolution from the PQ scale down to the QCD scale including cosmic strings.
2. *Harmonic approximation of the potential.* In our work we assume a quadratic axion potential without axion self-interactions in order to obtain linear evolution equations and decoupling of Fourier modes. In this way we cannot capture non-linear effects in locations with field values close to  $\pm\pi$ , which indeed are to be expected in this scenario. Numerical simulations performed in Refs. [8, 9] obtain very dense objects at those locations, which are not captured in our calculations. The open question remains of how likely those objects are and what their contribution to the total energy density is.
3. *Neglecting axions from cosmic strings and domain walls.* This is related to the previous item, since the harmonic approximation largely neglects the periodic nature of the axion field, and therefore the contribution to the axion energy density due to the decay of cosmic strings and the domain wall network cannot be described. Numerical simulations [14, 25, 26] show that this contribution can be substantial. Furthermore one expects this distribution not to be homogeneous and it may contribute also significantly to the power spectrum. Our approach neglects those effects and includes only the part from the re-alignment mechanism. The separation into re-alignment and string decay parts is largely artificial since both should follow from the same physics described by the non-linear field evolution. In the interpretation of our results one has to keep in mind that it includes only part of the power and additional contributions are expected.
4. *Gaussianity of density fluctuations.* In our method to calculate the distribution of collapsed objects we assume that the density fluctuation distribution is Gaussian,

with the variance determined by the power spectrum. The validity of this assumption is not obvious, due to order-one size of the fluctuations as well as non-linear effects mentioned in the items above. Some non-linearity can be implemented in principle in our formalism by considering higher-order correlation functions. But non-linear effects can lead to long non-Gaussian tails of the distribution, which can modify the mass function, particularly at large masses.

In view of those points, our results should be considered as a step towards the goal of obtaining a complete understanding of the minicluster distribution. It allows simple estimates and parameter dependence studies under the stated limitations. Future work will be dedicated to relaxing those assumptions.

## 5.2 Outlook and comments on observational consequences

An important open question is the subsequent evolution of the minicluster after turn-around. The two extreme possibilities are that either axions within the minicluster decohere and form a virialized system of dust-like particles [12], or the coherent field configuration collapses and admits a stable solution of the field equation under self-gravity, forming a so-called bose or axion star [41, 42], whose ultimate fate is currently under discussion, see e.g., Refs. [43–46]. While the investigation of the minicluster evolution after decoupling from the Hubble flow is beyond the scope of this work, our results on the relevant distribution of masses and sizes at turn-around provide useful input for such considerations.

Clearly the further evolution and the fate of miniclusters during the hierarchical formation of dark matter halos and the large scale structures has important consequences for axion dark matter searches. If we assume that a fraction  $f_{\text{MC}}$  of the total dark matter is in form of clumps with mass  $\sim 10^{-13}M_{\odot}$  their number density in our galaxy would be  $f_{\text{MC}} \times 10^{-44} \text{ cm}^{-3} \sim f_{\text{MC}} \times 10^{-5}/(1 \text{ AU})^3 \sim f_{\text{MC}}/\text{solar system}$ . The flux on Earth would be  $f_{\text{MC}} \times 10^{-37} \text{ cm}^{-2} \text{ s}^{-1}$ , and the frequency with which such a clump passes through a detector at Earth would be

$$\frac{f_{\text{MC}}}{t_{\text{Univ}}} \left( \frac{\text{clump size}}{10^6 \text{ km}} \right)^2 \quad (5.1)$$

with  $t_{\text{Univ}}$  being the age of the Universe. Hence the dark matter component bound in such objects is invisible to axion haloscopes such as the experiments described in Refs. [19, 20] and their expected event rate would be suppressed by a factor  $(1 - f_{\text{MC}})$ . On the other hand, if the final state of axion miniclusters is only loosely bound, they might be tidally disrupted in the galaxy, leading to potential signals in axion haloscopes [12]. The clumpy structure of dark matter halos due to the presence of miniclusters may lead to observable signals in femto-lensing [21] or micro-lensing [15, 16]. Again an important question to be answered in this context is about the size and masses of those objects today.

## Acknowledgements

We thank Arthur Hebecker, Jörg Jäckel and Javier Redondo for useful discussions. This project has received funding from the European Unions Horizon 2020 research and innovation programme under the Marie Skłodowska-Curie grant agreement No 674896 (Elusives). A.P. acknowledges the support by the DFG-funded Doctoral School KSETA.

## A Solving the equation of motion

In this appendix we discuss how we solve the equation of motion of the axion field. Since the Fourier modes evolve independently in the harmonic approximation, we can make the ansatz  $\theta_k(a) = \theta_k f_k(a)$ , eq. (3.8), with  $a$  being the scale factor. Then eq. (2.5) becomes an evolution equation for  $f_k$ :

$$\ddot{f}_k + 3H(T)\dot{f}_k + \omega_k^2(T)f_k = 0, \quad \omega_k^2(T) = \frac{k^2}{a^2} + m(T)^2. \quad (\text{A.1})$$

The temperature dependence of the Hubble rate  $H = \dot{a}/a$  is determined by the Friedmann equation

$$H^2 = \frac{8\pi}{3M_{\text{Pl}}^2}\rho, \quad (\text{A.2})$$

where  $M_{\text{Pl}}$  is the Planck mass and  $\rho$  is the energy density of the Universe. Since at the times we are interested in the Universe is radiation dominated,  $\rho$  can be expressed as

$$\rho = \frac{\pi^2}{30}g_\rho T^4. \quad (\text{A.3})$$

The relativistic degrees of freedom  $g_\rho$  depend on the temperature  $T$  of the Universe. In Ref. [28]  $g_\rho$  is determined by lattice calculations in the relevant range of temperatures. We use the tabulated values given therein and cubic spline interpolation to find  $g_\rho(T)$ . In the evolution equation for  $f_k$  not only the Hubble rate but also the axion mass  $m(T)^2 = \chi(T)/f_{\text{PQ}}^2$  depends on the temperature. To find  $m(T)$  we use the tabulated results for the topological susceptibility  $\chi(T)$  of the lattice calculations in Ref. [28] and employ cubic spline interpolation. With  $H(T)$  and  $m(T)$  at hand, it is convenient to rewrite the evolution equation in terms of temperature being the independent variable instead of time. With the initial condition  $f_k(T_i) = 1$  for all  $k$ , we can solve the resulting equation numerically to find  $f_k(T)$ .

Soon after  $T_{\text{osc}}$ , defined by  $3H(T_{\text{osc}}) = m(T_{\text{osc}})$ , rapid oscillations in  $f_k$  commence since the mass term dominates the evolution equation and we are dealing effectively with the equation of motion of an under-damped oscillator. This motivates a WKB ansatz for  $f_k$  of the form

$$f_k = 2A_k \cos \Phi_k \quad (T < T_{\text{osc}}) \quad (\text{A.4})$$

with slowly varying amplitude  $A_k$ :  $\dot{A}_k/A_k \ll \omega_k$ ,  $\ddot{A}_k/A_k \ll \omega_k^2$ . In this approximation the evolution of  $A_k$  respectively  $\Phi_k$  is determined by

$$\dot{A}_k + \frac{1}{2}A_k \left( 3H + \frac{\dot{\omega}_k}{\omega_k} \right) = 0, \quad (\text{A.5})$$

$$\dot{\Phi}^2 - \omega_k^2 = 0. \quad (\text{A.6})$$

The initial conditions for  $A_k$  and  $\Phi_k$  are found by matching the ansatz in eq. (A.4) and its derivative at a temperature  $T_{\text{WKB}} < T_{\text{osc}}$  to the result of the full numerical solution of

(A.1), i.e.,

$$2A_k(T_{\text{WKB}}) \cos \Phi_k(T_{\text{WKB}}) = f_k(T_{\text{WKB}}), \quad (\text{A.7})$$

$$2A_k(T_{\text{WKB}}) \sin \Phi_k(T_{\text{WKB}}) = \frac{\dot{f}_k(T_{\text{WKB}})}{\omega_k(T_{\text{WKB}})}. \quad (\text{A.8})$$

Supplemented with these initial conditions we can numerically solve eq. (A.5) and eq. (A.6) to find  $f_k(T)$  at any temperature  $T$ . For the matching temperature  $T_{\text{WKB}}$  between the WKB ansatz and the full numerical result we chose  $T_{\text{WKB}} = 0.5T_{\text{osc}}$ . We have checked that with this choice the WKB approximation provides an excellent fit to a full numerical solution. Note that for constant  $g_\rho$  and constant axion mass, eqs. (A.5) and (A.6) have a simple analytic solution. We decide to solve them numerically to implement the full  $T$  dependence of the relativistic degrees of freedom and the axion mass down to  $T_\star = 100$  MeV, where the power spectrum becomes constant.

## References

- [1] S. Weinberg, *A New Light Boson?*, *Phys. Rev. Lett.* **40** (1978) 223–226.
- [2] F. Wilczek, *Problem of Strong P and T Invariance in the Presence of Instantons*, *Phys. Rev. Lett.* **40** (1978) 279–282.
- [3] R. D. Peccei and H. R. Quinn, *Constraints Imposed by CP Conservation in the Presence of Instantons*, *Phys. Rev.* **D16** (1977) 1791–1797.
- [4] R. D. Peccei and H. R. Quinn, *CP Conservation in the Presence of Instantons*, *Phys. Rev. Lett.* **38** (1977) 1440–1443.
- [5] P. Sikivie, *Axion Cosmology*, *Lect. Notes Phys.* **741** (2008) 19–50, [[astro-ph/0610440](#)].
- [6] D. J. E. Marsh, *Axion Cosmology*, *Phys. Rept.* **643** (2016) 1–79, [[1510.07633](#)].
- [7] C. J. Hogan and M. J. Rees, *Axion Miniclusters*, *Phys. Lett.* **B205** (1988) 228–230.
- [8] E. W. Kolb and I. I. Tkachev, *Axion Miniclusters and Bose Stars*, *Phys. Rev. Lett.* **71** (1993) 3051–3054, [[hep-ph/9303313](#)].
- [9] E. W. Kolb and I. I. Tkachev, *Nonlinear Axion Dynamics and Formation of Cosmological Pseudosolitons*, *Phys. Rev.* **D49** (1994) 5040–5051, [[astro-ph/9311037](#)].
- [10] K. M. Zurek, C. J. Hogan, and T. R. Quinn, *Astrophysical Effects of Scalar Dark Matter Miniclusters*, *Phys. Rev.* **D75** (2007) 043511, [[astro-ph/0607341](#)].
- [11] I. I. Tkachev, *Fast Radio Bursts and Axion Miniclusters*, *JETP Lett.* **101** (2015), no. 1 1–6, [[1411.3900](#)]. [*Pisma Zh. Eksp. Teor. Fiz.*101,no.1,3(2015)].
- [12] P. Tinyakov, I. Tkachev, and K. Zioutas, *Tidal Streams from Axion Miniclusters and Direct Axion Searches*, *JCAP* **1601** (2016), no. 01 035, [[1512.02884](#)].
- [13] E. Hardy, *Miniclusters in the Axiverse*, *JHEP* **02** (2017) 046, [[1609.00208](#)].
- [14] J. Stadler, *The Formation of Axion Miniclusters*, *MSc thesis, Techn. Univ. Munich, Max Planck Inst. für Physik* (2016).
- [15] M. Fairbairn, D. J. E. Marsh, and J. Quevillon, *Searching for the QCD Axion with Gravitational Microlensing*, *Phys. Rev. Lett.* **119** (2017), no. 2 021101, [[1701.04787](#)].



- [16] M. Fairbairn, D. J. E. Marsh, J. Quevillon, and S. Rozier, *Structure Formation and Microlensing with Axion Miniclusters*, [1707.03310](#).
- [17] S. Davidson and T. Schwetz, *Rotating Drops of Axion Dark Matter*, *Phys. Rev.* **D93** (2016), no. 12 123509, [[1603.04249](#)].
- [18] Y. Bai, V. Barger, and J. Berger, *Hydrogen Axion Star: Metallic Hydrogen Bound to a QCD Axion Bec*, *JHEP* **12** (2016) 127, [[1612.00438](#)].
- [19] I. Stern, *ADMX Status*, *PoS ICHEP2016* (2016) 198, [[1612.08296](#)].
- [20] **MADMAX Working Group**, A. Caldwell, G. Dvali, B. Majorovits, A. Millar, G. Raffelt, et al., *Dielectric Haloscopes: a New Way to Detect Axion Dark Matter*, *Phys. Rev. Lett.* **118** (2017), no. 9 091801, [[1611.05865](#)].
- [21] E. W. Kolb and I. I. Tkachev, *Femtolensing and Picolensing by Axion Miniclusters*, *Astrophys. J.* **460** (1996) L25–L28, [[astro-ph/9510043](#)].
- [22] T. W. B. Kibble, *Topology of Cosmic Domains and Strings*, *J. Phys.* **A9** (1976) 1387–1398.
- [23] P. Sikivie, *Of Axions, Domain Walls and the Early Universe*, *Phys. Rev. Lett.* **48** (1982) 1156–1159.
- [24] R. L. Davis, *Cosmic Axions from Cosmic Strings*, *Phys. Lett.* **B180** (1986) 225–230.
- [25] T. Hiramatsu, M. Kawasaki, K. Saikawa, and T. Sekiguchi, *Production of Dark Matter Axions from Collapse of String-Wall Systems*, *Phys. Rev.* **D85** (2012) 105020, [[1202.5851](#)]. [Erratum: *Phys. Rev.*D86,089902(2012)].
- [26] M. Kawasaki, K. Saikawa, and T. Sekiguchi, *Axion Dark Matter from Topological Defects*, *Phys. Rev.* **D91** (2015), no. 6 065014, [[1412.0789](#)].
- [27] A. R. Zentner, *The Excursion Set Theory of Halo Mass Functions, Halo Clustering, and Halo Growth*, *Int. J. Mod. Phys.* **D16** (2007) 763–816, [[astro-ph/0611454](#)].
- [28] S. Borsanyi et al., *Calculation of the Axion Mass Based on High-Temperature Lattice Quantum Chromodynamics*, *Nature* **539** (2016), no. 7627 69–71, [[1606.07494](#)].
- [29] R. Kitano and N. Yamada, *Topology in QCD and the Axion Abundance*, *JHEP* **10** (2015) 136, [[1506.00370](#)].
- [30] G. Grilli di Cortona, E. Hardy, J. P. Vega, and G. Villadoro, *The QCD Axion, Precisely*, *JHEP* **01** (2016) 034, [[1511.02867](#)].
- [31] J. Preskill, M. B. Wise, and F. Wilczek, *Cosmology of the Invisible Axion*, *Phys. Lett.* **B120** (1983) 127–132.
- [32] L. F. Abbott and P. Sikivie, *A Cosmological Bound on the Invisible Axion*, *Phys. Lett.* **B120** (1983) 133–136.
- [33] M. Dine and W. Fischler, *The Not So Harmless Axion*, *Phys. Lett.* **B120** (1983) 137–141.
- [34] M. S. Turner, *Cosmic and Local Mass Density of Invisible Axions*, *Phys. Rev.* **D33** (1986) 889–896.
- [35] K. J. Bae, J.-H. Huh, and J. E. Kim, *Update of Axion CDM Energy*, *JCAP* **0809** (2008) 005, [[0806.0497](#)].
- [36] L. Visinelli and P. Gondolo, *Dark Matter Axions Revisited*, *Phys. Rev.* **D80** (2009) 035024, [[0903.4377](#)].

- [37] O. Wantz and E. P. S. Shellard, *Axion Cosmology Revisited*, *Phys. Rev.* **D82** (2010) 123508, [[0910.1066](#)].
- [38] W. H. Press and P. Schechter, *Formation of Galaxies and Clusters of Galaxies by Selfsimilar Gravitational Condensation*, *Astrophys. J.* **187** (1974) 425–438.
- [39] M. Maggiore and A. Riotto, *The Halo Mass Function from Excursion Set Theory. I. Gaussian Fluctuations with Non-Markovian Dependence on the Smoothing Scale*, *Astrophys. J.* **711** (2010) 907–927, [[0903.1249](#)].
- [40] E. W. Kolb and I. I. Tkachev, *Large Amplitude Isothermal Fluctuations and High Density Dark Matter Clumps*, *Phys. Rev.* **D50** (1994) 769–773, [[astro-ph/9403011](#)].
- [41] R. Ruffini and S. Bonazzola, *Systems of Selfgravitating Particles in General Relativity and the Concept of an Equation of State*, *Phys. Rev.* **187** (1969) 1767–1783.
- [42] S. L. Liebling and C. Palenzuela, *Dynamical Boson Stars*, *Living Rev. Rel.* **15** (2012) 6, [[1202.5809](#)].
- [43] D. G. Levkov, A. G. Panin, and I. I. Tkachev, *Relativistic Axions from Collapsing Bose Stars*, *Phys. Rev. Lett.* **118** (2017), no. 1 011301, [[1609.03611](#)].
- [44] T. Helfer, D. J. E. Marsh, K. Clough, M. Fairbairn, E. A. Lim, et al., *Black Hole Formation from Axion Stars*, *JCAP* **1703** (2017), no. 03 055, [[1609.04724](#)].
- [45] J. Eby, M. Leembruggen, P. Suranyi, and L. C. R. Wijewardhana, *Collapse of Axion Stars*, *JHEP* **12** (2016) 066, [[1608.06911](#)].
- [46] J. Eby, M. Leembruggen, P. Suranyi, and L. C. R. Wijewardhana, *QCD Axion Star Collapse with the Chiral Potential*, *JHEP* **06** (2017) 014, [[1702.05504](#)].